How brain reacts to targeted attack at a hub region

Wenyu Tu[1], Zilu Ma[2], Yuncong Ma[2] and Nanyin Zhang[1,2]*

[1] Neuroscience Program, The Huck Institutes of the Life Sciences, The Pennsylvania State University, University Park, PA 16802, USA

[2] Department of Biomedical Engineering, The Pennsylvania State University, University Park, PA 16802, USA

***Address for correspondence:**

Nanyin Zhang, PhD

Professor of Biomedical Engineering and Electrical Engineering

Lloyd & Dorothy Foehr Huck Chair in Brain Imaging

The Huck Institutes of the Life Sciences

The Pennsylvania State University

W-341 Millennium Science Complex, University Park, PA 16802, USA

Email: nuz2@psu.edu

Conflict of interest: none.

Keywords: DREADD, resting-state fMRI, default mode network, graph theory, awake, rat

Abstract

The architecture of brain networks has been extensively studied in multiple species. However, exactly how the brain network reconfigures when a local region stops functioning remains elusive. By combining chemogenetics and resting-state functional magnetic resonance imaging (rsfMRI) in awake rodents, we investigated the causal impact of acutely inactivating a hub region (i.e. dorsal anterior cingulate cortex) on brain network properties. We found that disrupting hub activity profoundly changed the function the default-mode network (DMN), and this change was associated with altered DMN-related behavior. Suppressing hub activity also impacted the topological architecture of the whole-brain network in network resilience, segregation and small worldness, but not network integration. This study has established a system that allows for mechanistically dissecting the relationship between local regions and brain network properties. Our data provide direct evidence supporting the hypothesis that acute dysfunction of a brain hub can cause large-scale network changes. This study opens an avenue of manipulating brain networks by controlling hub-node activity.

Introduction

The mammalian brain is a highly inter-connected network system with distributed brain regions orchestrating to support normal function and mediate complex behavior (*1*). The brain network is organized to maintain an optimal balance of information segregation and integration, which simultaneously maximizes the efficiency of distal communication via long-range connections and minimizes the wiring cost through clustered local processing ((*2, 3*), but also see (*4*)). Such organization is well conserved in multiple species including rodents, primates and humans (*5-7*).

It is becoming increasingly clear that altered brain network organization is tightly linked to brain disorders (*8-10*). However, the neural substrates causing these large-scale network changes remain unknown. A key hypothesis is the dysfunction of brain hub regions. Hubs are brain regions that have high degrees of connections with the rest of the brain (*11, 12*). Because of their central roles, dysfunction of hub nodes can change global integrative process, and has been hypothesized to be a direct cause of altered brain network properties and pathophysiology of brain disorders (*13-15*). For instance, brain network analysis in patients with Alzheimer's Disease showed that amyloid-beta deposition mainly accumulated in functional hubs (*16*). Therefore, comprehensively understanding the causal relationship between hub activity and brain network organization is critical. However, directly testing this hypothesis in humans is challenging, as selectively altering activity in a hub and dissecting its causal impact on brain networks are difficult.

This obstacle can be overcome in experimental animals using neuroscience tools like Designer Receptors Exclusively Activated by Designer Drugs (DREADDs) and resting

state functional magnetic resonance imaging (rsfMRI). DREADDs introduce genetically encoded modified muscarinic G-protein-coupled receptors into living neurons, which allow reversible *in vivo* manipulation of neuronal activity of a defined brain region for hours (*17*). rsfMRI measures brain-wide resting-state functional connectivity (RSFC), and provides comprehensive assessment of brain network properties (*5, 18*). Thus, combining these two techniques offers a system that allows us to characterize the reconfiguration of the brain network as the neural activity of a network node is selectively perturbed. Given the highly conserved brain network architecture in the mammalian brain (*5-7*), the results are translatable to humans.

Here we investigate the causal impact of manipulating a hub region, dorsal anterior cingulate cortex (dACC), on brain network function and organization, as well as behavior using an awake rodent model established in our lab (*19-22*). Imaging awake rodents avoids the confounding effects of anesthesia (*23-26*), and permits linking imaging to behavioral data (*21, 27*). dACC is selected because it is a known functional and anatomical hub in both human and rat brain (*11, 19, 28, 29*). We examine the impact of suppressing the dACC on the default mode network (DMN), which is composed of a group of distributed brain regions exhibiting higher activity at rest (*30, 31*). DMN function is tightly linked to self-referential mental activity in humans, and its abnormality has been linked to numerous brain disorders (*32, 33*). DMN has also been reported in rodents and primates (*6, 34-37*), although our understanding of DMN in animals is mostly limited to its anatomical resemblance to the DMN in humans (*6, 35*). Since dACC is a hub node in the rodent DMN (*34*), manipulating dACC activity provides an avenue for understanding the rodent DMN at the functional level. Our data show that suppressing the dACC disrupts

activity and connectivity across the whole DMN, and DMN activity changes are correlated with altered DMN-related behaviors. These data suggest that, like humans, DMN in rodents is a functional network with coordinated activity to mediate behavior. Furthermore, we demonstrate that suppressing the dACC impacts the organization of the whole-brain network including network resilience, segregation and small worldness, but not network integration. All these changes are absent in sham rats or when a non-hub region is suppressed. Taken together, this study provides direct measurement of the brain's response to targeted attack at a hub region, and presents a comprehensive framework demonstrating the pivotal role of hubs in the brain network.

Results

Animals were stereotactically injected with adeno-associated viruses (AAVs) expressing inhibitory G-protein coupled hM4Di receptor with a pan-neuronal synapsin promoter (AAV8.hSyn.hM4Di.mCherry, Addgene). After 4-6 weeks of recovery and protein expression (Fig. S1), animals received either Clozapine-N-Oxide (CNO) or saline 30 min before electrophysiology recording, rsfMRI scanning or behavioral tests. Saline and CNO sessions were separated by at least 3 days in a random order. The experimental procedure is summarized in Fig. 1.

DREADD suppressed both evoked and spontaneous neural activities in local regions.

We first validated the inhibitory effect of the DREADD using a visual stimulation paradigm (Fig.2). AAVs expressing inhibitory DREADD (AAV8.hSyn.hM4Di.mCherry, Addgene) were injected into the superior colliculus (SC). After recovery and DREADD

107 expression, neural activity in the SC was activated by visual stimuli (Figs. 2A-D, 1
108 flash/trial and 5 flashes/trial, 100ms per flash, 10 sec per trial, 15 trials per animal) and
109 measured by electrophysiology. SC firing rates were significantly reduced 30 min after
110 CNO injection (two-sample tests, 1 flash/trial, $t = 10.30$, $p = 8.8 \times 10^{-17}$, Figs. 2B & 2D; 5
111 flashes/trial, $t = 13.48$, $p = 4.1 \times 10^{-23}$, Fig. 2C & 2D). In addition, spontaneous neural
112 activities including spiking activity and local field potential (LFP), quantified by the
113 electrophysiology data 5s before the onset of visual stimulation in each trial, were
114 significantly dampened in CNO-injected rats (MUA: $t = 16.15$, $p = 1.041 \times 10^{-36}$; LFP: $t =$
115 5.84, $p = 8.6 \times 10^{-8}$; Figs. 2E, 2F & 2G). The LFP spectrograms after saline and CNO
116 injections in a representative rat were also shown in Fig. S2. These data collectively
117 confirmed the inhibitory effect of the DREADD on evoked and spontaneous neural
118 activities in rats.
119
120 *Suppressing the dACC reduced its rsfMRI signal, RSFC and local network organization.*
121 The bilateral dACC was transfected by inhibitory DREADDs under a pan-neuronal
122 synapsin promoter (AAV8.hSyn.hM4Di.mCherry, Addgene). Sham rats received a control
123 virus (AAV8-hsy-GFP, Addgene). Animals were scanned using rsfMRI twice in the awake
124 state, with each session starting 30 min after either CNO or saline injections. The two
125 imaging sessions were separated by at least 3 days with a randomized order. There was
126 no difference in motion level during rsfMRI scanning between CNO and saline injection
127 conditions in both DREADD and sham groups (Fig. S3).
128 Fig. 3A shows that DREADD suppression of the dACC reduced its resting-state
129 blood-oxygenation-level dependent (BOLD) amplitude (std normalized by mean, $t = 2.00$,

130 p = 0.048), again confirming the inhibitory effect of the DREADD on spontaneous neural
131 activity. Suppressing the dACC also affected its functional connectivity, reflected by
132 generally reduced RSFC in dACC seedmaps (for each map: one sample t test, p<0.0005,
133 linear mixed model, false discovery rate (FDR) corrected) after CNO injection relative to
134 saline injection (Fig. 3B). We further examined the impact of suppressing the dACC on
135 its local information processing, assessed by the modular structure, which is defined as
136 a group of nodes with significantly greater within-module connections than between-
137 module connections (*38*). The dACC-related module shrunk in size in DREADD rats after
138 CNO injection relative to saline injection at high graph densities (p < 0.05, linear mixed
139 model, Fig. 3E), suggesting that suppressing the dACC mainly dropped relatively weaker
140 connections in the dACC module.

141 In addition to dACC-related circuits, we assessed RSFC between regions of
142 interest (ROIs) across the whole brain. Multiple distributed connections exhibited altered
143 RSFC (two-sample t-tests, p < 0.05, linear mixed model, FDR corrected) with lower RSFC
144 in the majority of these connections (i.e. blue elements in the T map, Figs. 3C & 3D),
145 indicating that the impact of suppressing neural activity in a hub can go beyond the hub
146 itself and propagate to neural circuits across the whole brain. This ripple effect is
147 consistent with the report in human patients with focal brain lesions to critical locations
148 (*39*).

149 None of these changes (i.e. resting-state BOLD amplitude, dACC-related RSFC
150 and community size) were observed in sham rats when comparing CNO- to saline-
151 injection conditions (Fig. S4), which suggests that CNO had minimal off-target effects in
152 our system, ruling out its potential confounding effects on rsfMRI data (*40*).

153

154 *Suppressing dACC altered activity and connectivity in the DMN.*

155 Given that dACC is a major hub node in the functional network of DMN, we
156 examined the impact of inactivating the dACC on the DMN organization in awake rodents.
157 We first mapped the DMN using *fractional amplitude of low-frequency fluctuations* (fALFF),
158 defined by voxel-wise low-frequency spectrum power (0.01–0.08 Hz) normalized by the
159 full-spectrum power (*41*) of the rsfMRI signal. This well-established method measures the
160 amplitude of regional spontaneous brain activity. Thus, it can reliably identify brain regions
161 with higher activity at rest, and map the spatial pattern of the DMN (*41*).

162 Fig. 4 displays the DMN spatial maps in DREADD and sham rats after saline and
163 CNO injections, respectively. Brain regions highlighted in the network included the ACC,
164 posterior cingulate cortex (PCC), prelimbic cortex (PL), retrosplenial cortex (RSC), orbital
165 cortex (ORB), posterior parietal cortex (PPC), as well as subcortical regions of the basal
166 forebrain (BF) and hypothalamus (Hypo). This DMN pattern was reproduced with a
167 completely different analysis method (i.e. independent component analysis, Fig. S5)
168 previously used by other groups, and well agreed with the rodent DMN pattern reported
169 in the literature (*34-36*). Notably, we found that the BF was a prominent node in the rodent
170 DMN, which was not observed in other rodent DMN mapping studies, but was reported
171 in an electrophysiology study that demonstrated that the BF is a key DMN node and
172 critical in regulating DMN-related behaviors in rats (*42*).

173 Intriguingly, suppressing one node in the DMN (i.e. dACC) dampened the activity
174 of virtually the entire network (Fig. 4A, top row), reflected by reduced BOLD fALFF in the
175 ACC, dPCC, RSC, PL, PPC, BF and Hypo after CNO injection in DREADD-suppressed

176 rats (Fig. 4B, top row, $p < 0.05$, Family-wise error corrected, and Fig. 4C). Again, no
177 regions displayed reduced spontaneous activity in sham rats after CNO injection (Figs.
178 4A & 4B, bottom row). We also calculated RSFC between every pair of nodes in the DMN
179 including the dorsal and ventral ACC, dorsal and ventral PCC, RSC, ORB, PL, PPC, as
180 well as BF and Hypo (*34*) in both DREADD and sham rats after saline and CNO injections,
181 respectively (Fig. 4D). Cortical nodes generally displayed significantly reduced RSFC (p
182 < 0.05, FDR corrected, Figs. 4E & 4F), except that the RSC exhibited increased RSFC
183 with the PPC, BF and Hypo after CNO injection. In contrast, both subcortical nodes (BF
184 and Hypo) showed increased RSFC after dACC suppression (Figs. 4E & 4F). Taken
185 together, these data revealed that the DMN was significantly reorganized when dACC
186 activity was suppressed, suggesting that the rodent DMN is a functional network with
187 coordinated activity, and the dACC is a pivotal node in this network.
188
189 *Suppressing dACC altered DMN-related behaviors in animals.*
190 Considering that suppressing dACC significantly altered DMN activity in awake
191 rodents, we hypothesize that it also changes DMN-related behavior, measured by quiet
192 restfulness in rodents. Nair and colleagues demonstrated that quiet restfulness in home-
193 cage is characteristic behavior to DMN activity, evidenced by elevated neural activity in
194 the DMN, including ACC and BF, during this behavioral state (*42*). Robust DMN activation
195 during quiet restfulness was also reported in chimpanzees (*43*). Therefore, we evaluated
196 quiet restfulness, defined by continuous immobility for at least 2s, in our animals. After
197 either CNO or saline injection, the rat was put in the home cage for 45min and was video-
198 recorded. The animal's behavior was analyzed using behavioral tracking software (ANY-

maze, Stoelting Co., Wood Dale, IL). After CNO injection, quiet restfulness was significantly reduced in the rat (Fig. 5), reflected by significantly lower immobile time for at least 2s ($t = 3.991$, $p = 0.0009$), but higher distance travelled ($t = 4.294$, $p = 0.0004$), mean speed ($t = 4.811$, $p = 0.0001$) and total mobile time ($t = 3.991$, $p = 0.0009$). Rats also displayed significantly higher rearing after CNO injection ($t = 2.80$, $p = 0.01$), likely reflecting an increase in vigilance and/or exploratory behavior. Reduced quiet restfulness remained consistent during the last 15 min of testing, suggesting that these behavioral changes were not due to the environmental changes at the beginning of the test (Fig. S6).

We also examined whether DMN activity changes could explain altered DMN-related behaviors. In 8 animals, both behavioral and imaging data were collected after DREADD expression. Notably, both data were collected in the awake state, which permits linking results of these two measures. We found that fALFF changes in the dPCC and PL were significantly correlated to changes in all measures of DMN-related behavior including distance travelled (dPCC: $r = 0.80$, $p = 0.016$; PL: $r = 0.79$, $p = 0.019$), mean speed (dPCC: $r = 0.85$, $p = 0.0077$; PL: $r = 0.84$, $p = 0.0095$), mobile time (dPCC: $r = 0.74$, $p = 0.036$; PL: $r = 0.80$, $p = 0.017$) and immobile time (dPCC: $r = 0.74$, $p = 0.036$; PL: $r = 0.80$, $p = 0.017$). These data collectively demonstrate that dACC suppression alters DMN activity, and DMN activity changes can predict alteration in DMN-related behaviors.

Suppressing a hub node changed whole-brain network organization

We further investigated the effect of suppressing the dACC on the organization of the whole-brain network architecture in four aspects: network resilience, functional segregation, functional integration, and small-worldness. The rat brain was parcellated

222 into 68 bilateral ROIs based on the Swanson atlas (*44*). The whole-brain network was
223 constructed by calculating RSFC between every two ROIs, generating a RSFC matrix for
224 each animal at each condition. This RSFC matrix was then binarized based on graph
225 density. Graph topological parameters including assortativity, modularity, global efficiency,
226 and small-worldness were respectively calculated as a function of graph density.

227 Assortativity measures network resilience. Brain networks with high assortativity
228 are more resistant to local attack such as lesion and neurological degeneration (*12, 45*).
229 Fig. 6 shows that suppressing the dACC considerably reduced the network assortativity,
230 and as a consequence, the whole-brain network became more vulnerable (Fig. 6A).
231 Functional segregation, quantified by modularity, measures the network's ability of
232 specialized processing. We observed that dACC suppression decreased the modularity
233 of the global brain network, indicating reduced functional segregation (Fig. 6C). Global
234 efficiency measures functional integration, which assesses the ability to integrate
235 specialized information from distributed brain regions. Interestingly, suppressing the
236 dACC did not seem to affect the global efficiency (Fig. 6D). Small-worldness reflects the
237 ability to balance functional segregation and integration. Suppressing the dACC reduced
238 small-worldness of the whole-brain network (Fig. 6B). In summary, we observed that
239 suppression of the dACC affected global brain topology including network resilience,
240 network segregation and small-worldness, but not network integration.

241 As expected, DREADD suppression of the dACC significantly lowered its degree
242 (Fig. 7), suggesting that dACC lost its hubness in the network. Interestingly, the degree
243 of the ventral RSC was significantly increased after dACC suppression, which is
244 consistent with our data that some RSC connections increased their RSFC within the

245 DMN (Figs. 4E & 4F). Again, no changes in the degree of dACC or vRSC were observed
246 in sham rats (Fig. S7). These results indicate that a new hub can emerge when an existing
247 hub stops functioning, likely due to the compensatory mechanism.
248
249 *Suppression of a non-hub region did not change whole-brain network properties*
250 To determine whether aforementioned network changes depended on the specific
251 role of the node (i.e. hub versus non-hub), we also suppressed the activity in a non-hub
252 region—primary visual cortex (V1, bilateral) (*19*) using the same pan-neuronal inhibitory
253 DREADDs. After CNO injection, significantly reduced BOLD amplitude in V1 was
254 observed (Fig. 8A), which confirmed the inhibitory effect of DREADD in V1. However,
255 suppression of V1 did not affect fALFF in the DMN (Fig. S8), nor did it cause any whole-
256 brain topological changes including network resilience, functional segregation, functional
257 integration, or small-worldness (Figs. 8B-8E). Taken together, these data suggest that
258 attack on separate brain regions can have differential impact on brain network properties,
259 and brain networks are particularly vulnerable to targeted attack at hub nodes.
260

261 ## Discussion

262 For over a century, the neuroscience field has been tremendously moved forward
263 by the effort of examining the relationship between damage of specific brain regions and
264 loss of certain brain function. Classical examples include the discovery of the inferior
265 frontal gyrus in speech production by Paul Broca, and the left posterior temporal cortex
266 in language comprehension by Carl Wernicke. Despite this vital advancement,
267 converging evidence suggests that a large number of complex tasks involve numerous

268 cognitive processes and require integrated activity from multiple brain regions (*46*).
269 Therefore, brain function should be viewed as a network phenomenon.

270 By combining DREADDs and rsfMRI in an awake rodent model, we have
271 established a system that eables us to manipulate the activity in any brain region, and
272 measure the corresponding changes in brain-wide networks. This system allows for
273 mechanistically dissecting the causal relationship between a (or multiple) local brain
274 region(s) and brain network properties. In this study we specifically investigated the role
275 of a hub region (i.e. dACC) in brain networks. We found that disrupting hub activity
276 profoundly changed the function of the DMN (Figs 4), and this change was associated
277 with altered DMN-related behavior (Fig. 5). It also impacted the topological architecture
278 of the whole-brain network in terms of network resilience, segregation and small
279 worldness, but not network integration (Fig. 6). These data offer direct evidence
280 supporting the hypothesis that acute dysfunction of a brain hub can cause large-scale
281 network and behavioral changes. They also provide a comprehensive framework
282 documenting the differential impact of inactivating a hub versus a non-hub node on
283 network dynamics.

284

285 *Tight relationship between local regions and brain networks*

286 The activity in local brain regions can be manipulated using tools like
287 chemogenetic, optogenetic, pharmacological and lesion methods. Such perturbations are
288 often used to study the role of a specific brain region in behavior (*47*). Meanwhile, the
289 capacity of manipulating local brain regions can be tremendously expanded when
290 combining with neuroimaging approaches with a global field of view (e.g. fMRI), as the

291 causal impact of local region dysfunction on the rest of the interconnected network can
292 be monitored across the whole brain (*48*). For instance, using DREADDs and rsfMRI,
293 Grayson and colleagues showed that inactivating the amygdala disrupted communication
294 throughout the cortex in anesthetized monkeys (*49*). This observation echoes human
295 patient studies in which lesions of critical focal brain locations caused widespread
296 disruption of the brain modular structure (*39, 50*). These results collectively suggest tight
297 linkage between regional activity and large-scale network properties, and highlight the
298 importance of combining local perturbations and global network measurement. Uniquely,
299 in our study we specifically targeted a hub region to directly test the hypothesis that
300 dysfunction of hub nodes is a direct cause of altered brain network properties (*13-15*). In
301 addition, all data were collected in awake animals, which avoids the confounding effects
302 of anesthesia on brain network function, and permits direct association of network
303 features and behavioral changes. This nature also makes the findings translatable to
304 humans, considering numerous reports of large-scale brain network changes in human
305 brain disorders.
306
307 *DREADDs vs lesion*
308 There are several advantages choosing the DREADD over the lesion method for
309 our research purpose. First, DREADDs allow us to specifically and reversibly inhibit a
310 brain region with minimal damage. On the other hand, long-term damage in brain tissue
311 can decrease metabolism and alter local vascular structure. In addition, there can be
312 excessive blood flow in surrounding regions (*51*). All these factors will impact fMRI data
313 measurement and can confound RSFC results. Long-term lesion studies can also be

compounded by post-lesion neural plasticity changes resulting from the compensatory mechanism (i.e. secondary effects). Furthermore, most psychiatric disorders are linked to loss of function without tissue damage, making the DREADD method a better translatable model.

DMN in rodents – beyond anatomical resemblance with other species

We observed significant reconfiguration of the DMN after transiently inactivating one of its hub nodes (i.e. dACC) in awake rodents. DMN activity changes were also linked to altered DMN-related behaviors after dACC suppression. Although the DMN has been extensively studied in humans including its network structure, function and clinical implications, our understanding of the DMN in rodents is limited. The discovery of rodent DMN was mainly based on the anatomical resemblance of the network structure with the DMN in humans and primates (*35, 36*), but its functional role in behavior remains unclear. Nair and colleagues showed that the rat BF exhibited pronounced gamma oscillations during DMN-related behaviors and this activity was suppressed during active exploration of an unfamiliar environment (*42*), suggesting that the BF might be a key DMN node that regulates DMN activity. They further demonstrated that the BF controls DMN-related behaviors by affecting neural activity in the ACC. These results are highly consistent with our findings. First, we also observed prominent involvement of the BF in the rat DMN at baseline, which was missing in previous rodent DMN mapping studies (*34, 35*). Notably, the BF has strong connections with the cortex and subcortical regions like Hypo, and these connected regions substantially overlapped with the DMN revealed in our study (*52, 53*). Second, suppressing the dACC considerably dampened the DMN activity. This result

337 is consistent with the report that DMN hubs are mostly fragile (*54*). Third, reduced DMN-
338 related behaviors resulting from dACC suppression were correlated to activity changes in
339 DMN nodes. Taken together, these results support the concept that, like humans and
340 primates, the DMN in rodents is a functional network with coordinated neural activity from
341 distributed brain regions, and this network might support behavior related to internally
342 oriented brain states.
343
344 *Hubs and brain network topology*
345 The topological changes resulting from hub inactivation, including reduced network
346 resilience, segregation and small worldness, are important for our understanding of the
347 role of individual regions in the global brain network organization. A brain network can be
348 modeled as a graph composed of spatially distributed neuronal components as nodes
349 and anatomical or functional associations between components as edges (*2, 3*).
350 Topological features of the brain graph are critical in understanding inter-areal information
351 exchange in health and disease. Although the architecture of brain networks has been
352 extensively studied in multiple species (*5, 55-57*), it remains elusive whether different
353 types of nodes, such as hubs versus non-hubs, play distinct or similar roles in the topology
354 of the global brain network. Our data revealed that changes in a hub, but not a non-hub,
355 can significantly alter brain network topology. These results provide critical insight into
356 understanding the pathogenesis of neurological and psychiatric disorders, which indicate
357 that altered brain topological properties reported in these brain disorders might start from
358 dysfunction of certain hub nodes (*58*). Interestingly, our data showed that network
359 integration was intact after dACC inactivation, likely due to the compensatory effect of the

360 so-called ‘rich club organization’ in the rat brain (*19*). Another possible explanation is that
361 although the dACC has high centrality, it functions as a provincial hub as opposed to a
362 connector hub (*59*). These two types of hubs were demonstrated to have differential
363 impact on brain network properties (*39*), with connector hubs more affecting network
364 integration, and provincial hubs more affecting network segregation. Our result is
365 consistent with the report that the ACC belongs to the “segregation effect” class, as
366 reported in human lesion studies (*60*). Our data also support the notion that neural
367 network communication does not necessarily involve the shortest paths between nodes
368 (e.g. navigation routing) (*61*).
369

370 **Methods and Materials**

371 *Animals.*

372 44 adult male Long-Evans rats (300-500g) were used in the present study. Animals
373 were housed in Plexiglas cages. Food and water were provided *ad libitum*. The housing
374 room was maintained at an ambient temperature (22-24 ˚C) with a 12h light:12h dark
375 cycle. All experiments were approved by the Pennsylvania State University Institutional
376 Animal Care and Use Committee.
377

378 *Surgery.*

379 Aseptic stereotaxic surgery was conducted to infuse the virus to the brain. Rats
380 were anesthetized by intramuscular (IM) injections of ketamine (40 mg/kg) and xylazine
381 (12 mg/kg). Dexamethasone (0.5 mg/kg) and Baytril (2.5 mg/kg) were injected SQ to
382 prevent tissue inflammation and bacterial infections. During the surgery, respiration was

383 controlled by a ventilator with artificial oxygen. The heart rate was monitored by a pulse
384 oximetry (MouseSTAT® Jr., Kent Scientific Corporation), and the body temperature was
385 maintained at 37 ˚C with a warming pad (PhysioSuite, Kent Scientific Corporation). The
386 DREADD virus (AAV8-hSyn-hM4Di-mCherry, 1 μL at titer ≥ 3×10^{12} vg/mL, Addgene,
387 Watertown, MA) was bilaterally injected into the dACC (coordinates: AP +2, ML +/-0.5,
388 DV -1) and the primary visual cortex (coordinates: AP -6.5, ML +/-3.5, DV -1) for the hub
389 (n = 25) and non-hub (n = 8) groups, respectively [24]. Sham rats were injected with a
390 control virus (AAV8-hsy-GFP, 1 μL at titer ≥ 3×10^{12} vg/mL, Addgene, Watertown, MA, n
391 = 8)[24] into the dACC. In addition, separate animals used in the visual stimulation
392 experiment were unilaterally injected with AAV8-hSyn-hM4Di-mCherry (1 μL at titer ≥
393 3×10^{12} vg/mL, Addgene, Watertown, MA, n = 3) in the SC (coordinates: AP -7, ML +1.5,
394 DV -3). Rats were allowed to recover for at least four weeks.
395
396 *fMRI experiments:*
397 Before imaging, animals were acclimated to the MRI environment for 7 days in
398 order to minimize stress and motion during imaging. To better adapt the animal to the
399 restrainer and scanning environment, the acclimation period was gradually increased
400 from 15 min on Day 1 to 30 min on Day 2, 45 min on Day 3, and maintained at 60 min/day
401 for Days 4-7. Detailed procedures for acclimation can be found from our previous
402 publications (*62, 63*). A similar approach to imaging awake animals has also been
403 adopted by other research groups in multiple species (*64-66*). CNO (1mg/kg in saline,
404 dissolved in DMSO, Sigma-Aldrich, St. Louis, MO) or saline (with DMSO) was IP injected
405 30 min before rsfMRI data acquisition, at a random order with at least three days apart.

406 All imaging sections were conducted at the High Field MRI Facility at the
407 Pennsylvania State University on a 7T Bruker 70/30 BioSpec running ParaVision 6.0.1
408 (Bruker, Billerica, MA). rsfMRI data were acquired at the awake state using T2*-weighted
409 gradient-echo rsfMRI images using the echo-planar-imaging (EPI) sequence with the
410 following parameters: repetition time = 1000ms; echo time = 15ms; matrix size = 64×64;
411 field of view = 3.2 × 3.2 cm^2; slice number = 20; slice thickness = 1mm; flip angle = 60;
412 600 volume each run. Three runs were acquired each rsfMRI session. Raw EPI images
413 were shown in Fig. S9.
414
415 *Data analysis:*
416 All acquired image data were aligned to a defined atlas using Medical Image
417 Visualization and Analysis software (MIVA, http://ccni.wpi.edu/), and then subjected to
418 motion correlation (SPM12), spatial smoothing (Gaussian kernel, full-width at half-
419 maximum = 1 mm), voxel-wise nuisance regression of motion parameters, as well as the
420 signals from the white matter and ventricles, and bandpass filtering (0.01-0.1Hz). Before
421 these steps, rsfMRI volumes with relative framewise displacement (FD) > 0.25 mm and
422 the preceding and following volumes were removed. In addition, the first 10 volumes of
423 each rsfMRI scan were discarded to ensure steady state of magnetization. rsfMRI scans
424 with > 15% volumes discarded were removed from further analysis.
425 fALFF was determined by calculating the ratio of the power in the low-frequency
426 range (0.01–0.08 Hz) to that of the full spectrum (0–0.25 Hz). For each voxel, the time
427 course was transformed to the frequency domain using FFT. We calculated the ratio
428 between the square root of power in the range of 0.01–0.08 Hz and that across the entire

429 frequency range. fALFF changes after DREADD inhibition were obtained using voxel-
430 wise two-sample t-tests with family wise error correction ($P<0.05$, FWE corrected)
431 between data acquired after CNO injection versus saline injection.

432 Seed RSFC maps were generated using seed-based correlation analysis. Pearson
433 cross-correlation coefficients between the regionally averaged time course from all voxels
434 inside the seed and time courses of individual voxels were calculated. The corresponding
435 correlation coefficients were Fisher transformed, averaged across all scans and animals
436 in each group, and transformed back to r values.

437 The whole-brain RSFC network was constructed by parcellating the rat brain into
438 68 anatomical ROIs based on the Swanson Atlas (*44*), which were also grouped into 10
439 functional systems including amygdala complex, striatum, hypothalamus, hippocampus,
440 thalamus, sensory-motor cortex, polymodal association cortex, brainstem, pallidum, and
441 retro-hippocampal regions. RSFC between each pair of ROIs was calculated by Pearson
442 correlation of regionally averaged time series of the ROIs.

443 A hub score of each node ranged from 0-4 was determined by the number of the
444 following four criteria the node met: (1) 20% highest degree; (2) 20% highest
445 betweenness centrality; (3) 20% lowest characteristic path length; (4) 20% lowest local
446 clustering coefficient.

447 Topological parameters of the whole-brain network including the modularity, global
448 efficiency, small-worldness and assortativity were calculated on binarized network across
449 the graph density ranging from 0.15 to 0.45 with a step of 0.05 using the brain connectivity
450 toolbox (BCT) [30] based on the following equations:

451 *Assortativity (45):*

$$r = \frac{l^{-1}\sum_{(x,y\in L)} k_x k_y - [l^{-1}\sum_{(x,y\in L)} \frac{1}{2}(k_x + k_y)]^2}{l^{-1}\sum_{(x,y\in L)} \frac{1}{2}(k_x^2 + k_y^2) - [l^{-1}\sum_{(x,y\in L)} \frac{1}{2}(k_x + k_y)]^2}$$

where k_x, k_y is the degree of node x and y on two opposite ends of an edge; L is the set of all edges within the network, and l is the total number of edges.

Modularity (67):

$$Q = \sum_{i\in M}[e_{ii} - (\sum_{j\in M} e_{ij})^2]$$

where M represents a set of non-overlapping modules, and e_{ij} is the proportion of between-modules connections of module i and j; e_{ii} is the proportion of within-modules connections of module i.

Global efficiency (68):

$$E = \frac{1}{n}\sum_{i\in N}\frac{\sum_{y\in N, y\neq x} d_{xy}^{-1}}{n-1}$$

where n is the total number of nodes; N is the set of all nodes. d_{xy} is the shortest path length between nodes x and y.

Small-worldness (69):

$$S = \frac{C/C_{rand}}{L/L_{rand}}$$

where C and C_{rand} are the clustering coefficients of the testing network and a random network, respectively; L and L_{rand} are the characteristic path lengths of the testing network and a random network.

At each graph density, all topological parameters were determined for each scan. Changes in each parameter was determined by two-sample t-tests (linear mixed model)

473 between the CNO injection and saline injection conditions.

474

475 *Behavioral Test*

476 Animals underwent two behavioral sessions with either CNO or saline injection
477 with a random order separated by at least 7 days. Each session was composed of a 45
478 min home-cage test. Before the test, the animal was acclimated to the behavioral room
479 for 15 min, followed by either CNO (1mg/kg) or saline injection. The animal was then put
480 back to its home-cage in the behavioral room for 45 min. Behaviors including the total
481 distance traveled, mean speed, time of mobility and time of immobility for at least 2s were
482 recorded by an infrared camera and analyzed by behavioral tracking software (ANY-maze,
483 Stoelting Co., Wood Dale, IL).

484

485 *Electrophysiology*.

486 Electrophysiology recordings were conducted in animals with inhibitory DREADD
487 expressed in the SC. Rats were initially anesthetized by IM injections of ketamine (40
488 mg/kg) and xylazine (12 mg/kg). An electrode (Neuronexus, Ann Arbor, MI) was then
489 inserted into the SC to measure visually-evoked neuronal response to light stimulation
490 produced by a blue laser source (100 mW, 473 nm, Opto Engine) coupled with an optic
491 fiber, which was placed 5 cm away from the contralateral eye. Before recording, rats were
492 injected with either saline or CNO in each session. During recording, light anesthesia was
493 maintained using isoflurane (~0.75%). Each session included 15 trials of visual
494 stimulation, presented as a single light flash (100 ms per flash) or five flashes (100 ms
495 each flash, 100 ms inter-flash interval) every 10 s. Light stimulation was controlled by a

496 custom Labview program. The electrophysiological signal was amplified and sampled at
497 25 kHz using a Neuronexus recording system (Neuronexus, Ann Arbor, MI). Raw data
498 were bandpass filtered (MUA: 300-3000 Hz, LFP: 3-300 Hz). Spikes larger than three
499 times of the standard deviation of electrophysiological signal were detected and clustered
500 at a bin size of 50 ms in peristimulus-timed histograms (PSTHs).
501
502 *Histology.*
503 After electrophysiology, animal was perfused with saline followed by 4% PFA
504 solution. The brain was taken out carefully and stored in solution with 4%
505 paraformaldehyde and 20% sucrose. After fixation, the brain was sliced into 60μm slices.
506 Fluorescent expression in the injection site was examined under microscopy.
507
508 **Acknowledgments**
509 We would like to thank Yikang Liu and David Dopfel for their technical support. The
510 present study was partially supported by National Institute of Neurological Disorders and
511 Stroke Grant R01NS085200 (PI: Nanyin Zhang, PhD) and National Institute of Mental
512 Health Grant R01MH098003 and RF1MH114224 (PI: Nanyin Zhang, PhD).
513
514 **Author Contributions**: N.Z. designed the research; W.T., Z.M. and Y.M. performed
515 animal experiments; W.T. and Y.M. performed data analysis; N.Z. and W.T. wrote the
516 paper.
517
518 **Conflict of interest**: the Authors declare no competing interests.
519

Data availability: Data supporting the findings of this manuscript are available from the corresponding author upon reasonable request.

References:

1. E. T. Bullmore, D. S. Bassett, Brain graphs: graphical models of the human brain connectome. *Annu Rev Clin Psychol* **7**, 113-140 (2011).
2. E. Bullmore, O. Sporns, Complex brain networks: graph theoretical analysis of structural and functional systems. *Nat Rev Neurosci* **10**, 186-198 (2009).
3. E. Bullmore, O. Sporns, The economy of brain network organization. *Nat Rev Neurosci* **13**, 336-349 (2012).
4. R. F. Betzel, D. S. Bassett, Specificity and robustness of long-distance connections in weighted, interareal connectomes. *Proc Natl Acad Sci U S A* **115**, E4880-E4889 (2018).
5. Z. Liang, J. King, N. Zhang, Uncovering intrinsic connectional architecture of functional networks in awake rat brain. *J Neurosci* **31**, 3776-3783 (2011).
6. J. L. Vincent *et al.*, Intrinsic functional architecture in the anaesthetized monkey brain. *Nature* **447**, 83-86 (2007).
7. J. Wang, X. Zuo, Y. He, Graph-based network analysis of resting-state functional MRI. *Front Syst Neurosci* **4**, 16 (2010).
8. Y. Liu *et al.*, Disrupted small-world networks in schizophrenia. *Brain* **131**, 945-961 (2008).
9. D. S. Bassett, E. T. Bullmore, Human brain networks in health and disease. *Curr Opin Neurol* **22**, 340-347 (2009).
10. A. Fornito, A. Zalesky, M. Breakspear, The connectomics of brain disorders. *Nat Rev Neurosci* **16**, 159-172 (2015).
11. M. P. van den Heuvel, O. Sporns, Network hubs in the human brain. *Trends Cogn Sci* **17**, 683-696 (2013).
12. M. Rubinov, O. Sporns, Complex network measures of brain connectivity: uses and interpretations. *Neuroimage* **52**, 1059-1069 (2010).
13. N. A. Crossley *et al.*, The hubs of the human connectome are generally implicated in the anatomy of brain disorders. *Brain* **137**, 2382-2395 (2014).
14. J. Alstott, M. Breakspear, P. Hagmann, L. Cammoun, O. Sporns, Modeling the impact of lesions in the human brain. *PLoS Comput Biol* **5**, e1000408 (2009).
15. T. Takahashi *et al.*, Progressive gray matter reduction of the superior temporal gyrus during transition to psychosis. *Arch Gen Psychiatry* **66**, 366-376 (2009).
16. R. L. Buckner *et al.*, Cortical hubs revealed by intrinsic functional connectivity: mapping, assessment of stability, and relation to Alzheimer's disease. *J Neurosci* **29**, 1860-1873 (2009).

17. B. N. Armbruster, X. Li, M. H. Pausch, S. Herlitze, B. L. Roth, Evolving the lock to fit the key to create a family of G protein-coupled receptors potently activated by an inert ligand. *Proc Natl Acad Sci U S A* **104**, 5163-5168 (2007).
18. B. Biswal, F. Z. Yetkin, V. M. Haughton, J. S. Hyde, Functional connectivity in the motor cortex of resting human brain using echo-planar MRI. *Magn Reson Med* **34**, 537-541 (1995).
19. Z. Ma *et al.*, Functional atlas of the awake rat brain: A neuroimaging study of rat brain specialization and integration. *Neuroimage* **170**, 95-112 (2018).
20. N. Zhang *et al.*, Mapping resting-state brain networks in conscious animals. *J Neurosci Methods* **189**, 186-196 (2010).
21. D. Dopfel *et al.*, Individual variability in behavior and functional networks predicts vulnerability using an animal model of PTSD. *Nat Commun* **10**, 2372 (2019).
22. Z. Ma, N. Zhang, Temporal transitions of spontaneous brain activity. *eLife* **7**, (2018).
23. Y. R. Gao *et al.*, Time to wake up: Studying neurovascular coupling and brain-wide circuit function in the un-anesthetized animal. *Neuroimage*, (2016).
24. C. Hamilton, Y. Ma, N. Zhang, Global reduction of information exchange during anesthetic-induced unconsciousness. *Brain structure & function* **222**, 3205-3216 (2017).
25. Z. Liang, J. King, N. Zhang, Intrinsic organization of the anesthetized brain. *J Neurosci* **32**, 10183-10191 (2012).
26. Y. Ma, C. Hamilton, N. Zhang, Dynamic Connectivity Patterns in Conscious and Unconscious Brain. *Brain connectivity* **7**, 1-12 (2017).
27. Z. Liang, J. King, N. Zhang, Neuroplasticity to a single-episode traumatic stress revealed by resting-state fMRI in awake rats. *Neuroimage* **103**, 485-491 (2014).
28. M. P. van den Heuvel, L. H. Scholtens, M. A. de Reus, Topological organization of connectivity strength in the rat connectome. *Brain structure & function* **221**, 1719-1736 (2016).
29. G. Bush, P. Luu, M. I. Posner, Cognitive and emotional influences in anterior cingulate cortex. *Trends Cogn Sci* **4**, 215-222 (2000).
30. D. A. Gusnard, M. E. Raichle, M. E. Raichle, Searching for a baseline: functional imaging and the resting human brain. *Nat Rev Neurosci* **2**, 685-694 (2001).
31. M. E. Raichle *et al.*, A default mode of brain function. *Proc Natl Acad Sci U S A* **98**, 676-682 (2001).
32. D. Zhang, M. E. Raichle, Disease and the brain's dark energy. *Nat Rev Neurol* **6**, 15-28 (2010).
33. S. Whitfield-Gabrieli, J. M. Ford, Default mode network activity and connectivity in psychopathology. *Annu Rev Clin Psychol* **8**, 49-76 (2012).
34. L. M. Hsu *et al.*, Constituents and functional implications of the rat default mode network. *Proc Natl Acad Sci U S A* **113**, E4541-4547 (2016).

35. H. Lu *et al.*, Rat brains also have a default mode network. *Proc Natl Acad Sci U S A* **109**, 3979-3984 (2012).
36. J. M. Stafford *et al.*, Large-scale topology and the default mode network in the mouse connectome. *Proc Natl Acad Sci U S A* **111**, 18745-18750 (2014).
37. Z. C. Zhou *et al.*, Resting state network topology of the ferret brain. *Neuroimage* **143**, 70-81 (2016).
38. M. E. Newman, Modularity and community structure in networks. *Proc Natl Acad Sci U S A* **103**, 8577-8582 (2006).
39. C. Gratton, E. M. Nomura, F. Perez, M. D'Esposito, Focal brain lesions to critical locations cause widespread disruption of the modular organization of the brain. *Journal of cognitive neuroscience* **24**, 1275-1285 (2012).
40. J. L. Gomez *et al.*, Chemogenetics revealed: DREADD occupancy and activation via converted clozapine. *Science* **357**, 503-507 (2017).
41. Q. H. Zou *et al.*, An improved approach to detection of amplitude of low-frequency fluctuation (ALFF) for resting-state fMRI: fractional ALFF. *J Neurosci Methods* **172**, 137-141 (2008).
42. J. Nair *et al.*, Basal forebrain contributes to default mode network regulation. *Proc Natl Acad Sci U S A* **115**, 1352-1357 (2018).
43. S. K. Barks, L. A. Parr, J. K. Rilling, The default mode network in chimpanzees (Pan troglodytes) is similar to that of humans. *Cereb Cortex* **25**, 538-544 (2015).
44. L. W. Swanson, *Brain Maps: Structure of the Rat Brain.*, (Elsevier, 2004).
45. M. E. Newman, Assortative mixing in networks. *Phys Rev Lett* **89**, 208701 (2002).
46. R. Liegeois *et al.*, Resting brain dynamics at different timescales capture distinct aspects of human behavior. *Nat Commun* **10**, 2317 (2019).
47. P. D. Whissell, S. Tohyama, L. J. Martin, The Use of DREADDs to Deconstruct Behavior. *Front Genet* **7**, 70 (2016).
48. J. H. Lee *et al.*, Global and local fMRI signals driven by neurons defined optogenetically by type and wiring. *Nature* **465**, 788-792 (2010).
49. D. S. Grayson *et al.*, The Rhesus Monkey Connectome Predicts Disrupted Functional Networks Resulting from Pharmacogenetic Inactivation of the Amygdala. *Neuron* **91**, 453-466 (2016).
50. D. E. Warren *et al.*, Network measures predict neuropsychological outcome after brain injury. *Proc Natl Acad Sci U S A* **111**, 14247-14252 (2014).
51. C. Rorden, H. O. Karnath, Using human brain lesions to infer function: a relic from a past era in the fMRI age? *Nat Rev Neurosci* **5**, 813-819 (2004).
52. M. R. Gielow, L. Zaborszky, The Input-Output Relationship of the Cholinergic Basal Forebrain. *Cell Rep* **18**, 1817-1830 (2017).
53. L. J. Agostinelli, J. C. Geerling, T. E. Scammell, Basal forebrain subcortical projections. *Brain structure & function* **224**, 1097-1117 (2019).

54. L. L. Gollo *et al.*, Fragility and volatility of structural hubs in the human connectome. *Nat Neurosci* **21**, 1107-1116 (2018).
55. A. Liska, A. Galbusera, A. J. Schwarz, A. Gozzi, Functional connectivity hubs of the mouse brain. *Neuroimage* **115**, 281-291 (2015).
56. A. M. Belcher *et al.*, Large-scale brain networks in the awake, truly resting marmoset monkey. *J Neurosci* **33**, 16796-16804 (2013).
57. D. S. Bassett, E. Bullmore, Small-world brain networks. *Neuroscientist* **12**, 512-523 (2006).
58. W. W. Seeley, R. K. Crawford, J. Zhou, B. L. Miller, M. D. Greicius, Neurodegenerative diseases target large-scale human brain networks. *Neuron* **62**, 42-52 (2009).
59. R. Guimera, L. A. Nunes Amaral, Functional cartography of complex metabolic networks. *Nature* **433**, 895-900 (2005).
60. B. Yuan *et al.*, Brain hubs in lesion models: Predicting functional network topology with lesion patterns in patients. *Sci Rep* **7**, 17908 (2017).
61. C. Seguin, M. P. van den Heuvel, A. Zalesky, Navigation of brain networks. *Proc Natl Acad Sci U S A* **115**, 6297-6302 (2018).
62. D. Dopfel, N. Zhang, Mapping stress networks using functional magnetic resonance imaging in awake animals. *Neurobiol Stress* **9**, 251-263 (2018).
63. Z. Liang, J. King, N. Zhang, Anticorrelated resting-state functional connectivity in awake rat brain. *Neuroimage* **59**, 1190-1199 (2012).
64. E. Bergmann, G. Zur, G. Bershadsky, I. Kahn, The Organization of Mouse and Human Cortico-Hippocampal Networks Estimated by Intrinsic Functional Connectivity. *Cereb Cortex* **26**, 4497-4512 (2016).
65. K. Yoshida *et al.*, Physiological effects of a habituation procedure for functional MRI in awake mice using a cryogenic radiofrequency probe. *J Neurosci Methods* **274**, 38-48 (2016).
66. P. C. Chang *et al.*, Novel method for functional brain imaging in awake minimally restrained rats. *J Neurophysiol* **116**, 61-80 (2016).
67. M. E. Newman, Fast algorithm for detecting community structure in networks. *Phys Rev E Stat Nonlin Soft Matter Phys* **69**, 066133 (2004).
68. V. Latora, M. Marchiori, Efficient behavior of small-world networks. *Phys Rev Lett* **87**, 198701 (2001).
69. M. D. Humphries, K. Gurney, Network 'small-world-ness': a quantitative method for determining canonical network equivalence. *PLoS One* **3**, e0002051 (2008).

673 **Figure Captions.**

674 **Figure 1**. *Schematic diagram of the experimental paradigm.*

675 **Figure 2**. *Validation of the inhibitory effect of DREADDs*. **A**) Visual stimulation paradigm;
676 Spiking activity in the SC in response to **B**) 1 flash (100ms/flash) and **C**) 5 flashes
677 (100ms/flash) of light stimulation after saline and CNO injections (15 trials per animal, per
678 condition, number of animals = 3); **D**) DREADD suppressed evoked firings (two-sample
679 tests, 1 flash/trial, $t = 10.30$, $p = 8.8 \times 10^{-17}$; 5 flashes/trial, $t = 13.48$, $p = 4.1 \times 10^{-23}$); **E**)
680 DREADD suppressed spontaneous firings during 5s before visual stimulation ($t = 16.15$,
681 $p = 1.041 \times 10^{-36}$); **F**) Averaged spectrograms after saline (left) and CNO (right) injections;
682 **G**) Chemogenetic inhibition reduced local field potential power (3-300Hz) in the SC ($t =$
683 5.84, $p = 8.6 \times 10^{-8}$). ***: $p < 0.005$.

684 **Figure 3.** *Suppressing dACC reduced its spontaneous BOLD signal, RSFC, and local*
685 *network structure.* **A**) Amplitude of spontaneous BOLD activity in DREADD (19 animals,
686 78 scans) and sham groups (8 animals, 41scans); **B**) Averaged seedmaps after saline
687 and CNO injections (for each map: one-sample t-test, linear mixed model, $p < 0.0005$,
688 FDR corrected); **C**) Left: averaged ROI-wise RSFC matrices after saline and CNO
689 injections in the DREADD group. Right: connections exhibiting significant RSFC change
690 (two-sample t-test, linear mixed model, $p < 0.05$, FDR corrected). **D**) These connections
691 were grouped into multiple brain systems. Line thickness represents the total number of
692 connections with significant RSFC changes between the two systems; **E**) The size of the
693 dACC-associated community structure as a function of graph density in the DREADD
694 group after saline and CNO injections (two-sample t-test, linear mixed model). *: $p < 0.05$;
695 **: $p < 0.01$.

696 **Figure 4.** *Suppressing dACC disrupted activity across the DMN.* **A**) DMN constructed
697 using fractional amplitude of low-frequency fluctuations (fALFF) after saline and CNO
698 injections; **B**) Voxel-wise fALFF changes after DREADD inhibition ($p < 0.05$, linear mixed
699 model, family-wise error corrected); C) ROI-wise fALFF changes after DREADD inhibition
700 (*: $p < 0.05$; **: $p < 0.01$; ***: $p < 0.005$; #: $p = 0.11$). **D**) RSFC between DMN regions in the
701 DREADD and sham groups after saline and CNO injections, respectively; **E**) RSFC
702 changes between DMN nodes after dACC inhibition ($p < 0.05$, linear mixed model, FDR
703 corrected); **F**) Negative and positive RSFC changes after dACC inhibition ($p < 0.05$, linear
704 mixed model, FDR corrected).

705 **Figure 5**. *Suppressing dACC changed DMN-related behavior (n=14).* **A**) Total distance
706 traveled in homecage (45 min); **B**) Mean speed; **C**) Total mobile time; **D**) Total immobile
707 time for at least 2s. **E**) Total rearing behavior. *: $p < 0.05$; ***: $p < 0.005$. **F**) Correlations
708 of dPCC activity and DMN-related behaviors. **G**) Correlations of PL activity and DMN-
709 related behaviors.

710 **Figure 6**. *Suppressing a hub node changed whole-brain network topology.* **A**) Network
711 resilience; **B**) Small-worldness; **C**) Network segregation; **D**) Network integration. Linear
712 mixed model; DREADD: n = 19, 78 scans; sham: n = 8, 41 scans. *: $p < 0.05$; **: $p < 0.01$.

713 **Figure 7**. *New hub emerged after the inactivation of an existing hub*. **A**) Hub scores
714 without and with dACC inactivation, respectively; **B**) The degree of dACC and ventral
715 RSC without and with dACC inactivation (linear mixed model; n = 19, 78 scans). *: $p <$
716 0.05; **: $p < 0.01$; ***: $p < 0.005$.

717 **Figure 8.** *Suppressing a non-hub node did not change whole-brain network topology.* **A**)
718 Amplitude of spontaneous BOLD activity in the primary visual cortex after CNO and saline
719 injections ($p < 0.05$, n=8, 66 scans); **B**) Network resilience; **C**) Small-worldness; **D**)
720 Network segregation; **E**) Network integration.

721

722 **Figures.**

723

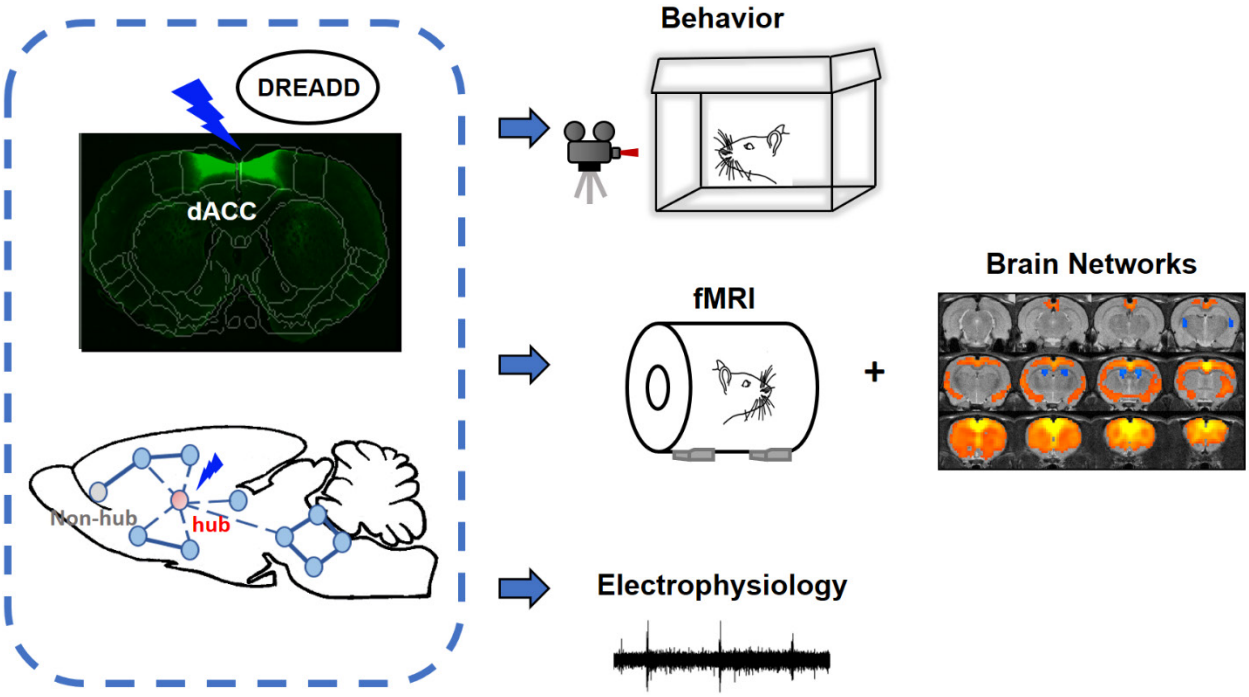

724

725 **Figure 1**. *Schematic diagram of the experimental paradigm.*

726

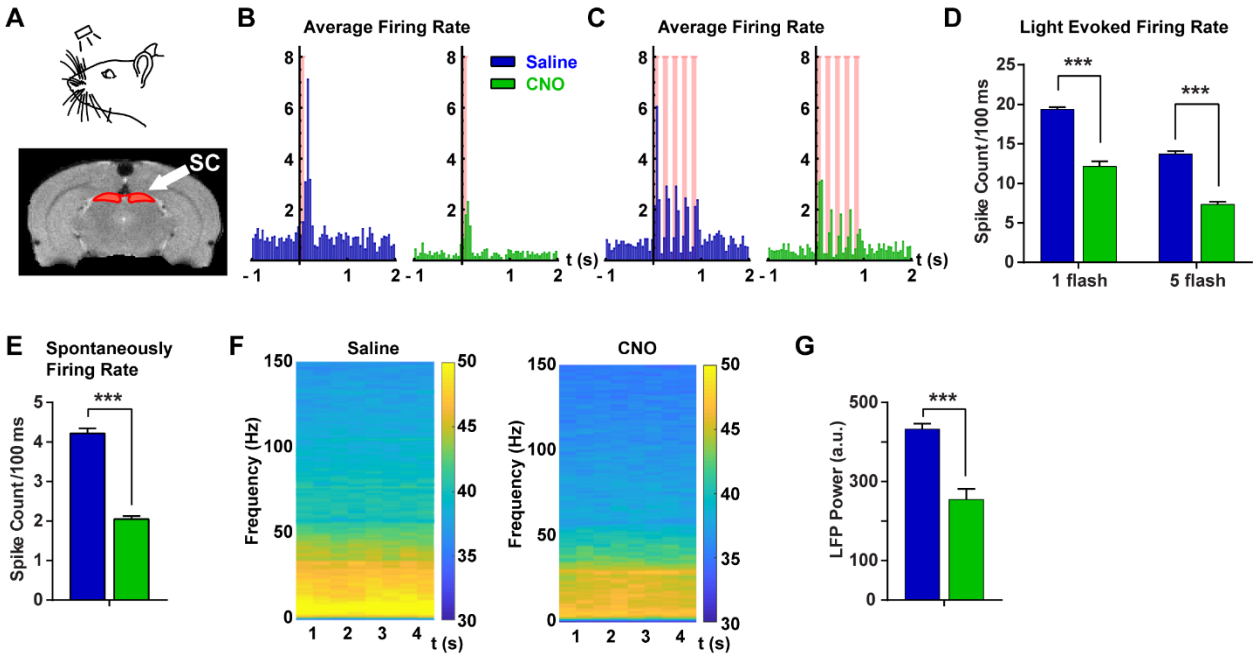

Figure 2. *Validation of the inhibitory effect of DREADDs*. **A**) Visual stimulation paradigm; Spiking activity in the SC in response to **B**) 1 flash (100ms/flash) and **C**) 5 flashes (100ms/flash) of light stimulation after saline and CNO injections (15 trials per animal, per condition, number of animals = 3); **D**) DREADD suppressed evoked firings (two-sample tests, 1 flash/trial, $t = 10.30$, $p = 8.8 \times 10^{-17}$; 5 flashes/trial, $t = 13.48$, $p = 4.1 \times 10^{-23}$); **E**) DREADD suppressed spontaneous firings during 5s before visual stimulation ($t = 16.15$, $p = 1.041 \times 10^{-36}$); **F**) Averaged spectrograms after saline (left) and CNO (right) injections; **G**) Chemogenetic inhibition reduced local field potential power (3-300Hz) in the SC ($t = 5.84$, $p = 8.6 \times 10^{-8}$). ***: $p < 0.005$.

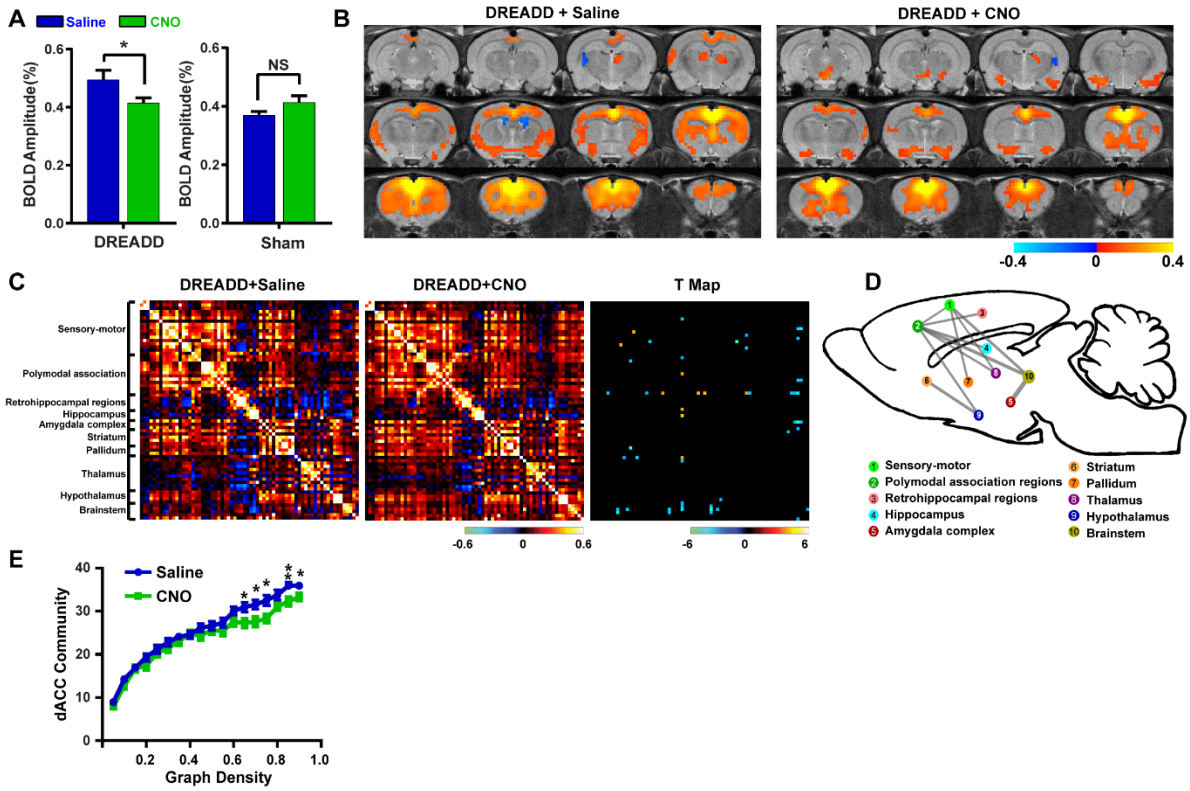

Figure 3. *Suppressing dACC reduced its spontaneous BOLD signal, RSFC, and local network structure.* **A**) Amplitude of spontaneous BOLD activity in DREADD (19 animals, 78 scans) and sham groups (8 animals, 41scans); **B**) Averaged seedmaps after saline and CNO injections (for each map: one-sample t-test, linear mixed model, $p < 0.0005$, FDR corrected); **C**) Left: averaged ROI-wise RSFC matrices after saline and CNO injections in the DREADD group. Right: connections exhibiting significant RSFC change (two-sample t-test, linear mixed model, $p < 0.05$, FDR corrected). **D**) These connections were grouped into multiple brain systems. Line thickness represents the total number of connections with significant RSFC changes between the two systems; **E**) The size of the dACC-associated community structure as a function of graph density in the DREADD group after saline and CNO injections (two-sample t-test, linear mixed model). *: $p < 0.05$; **: $p < 0.01$.

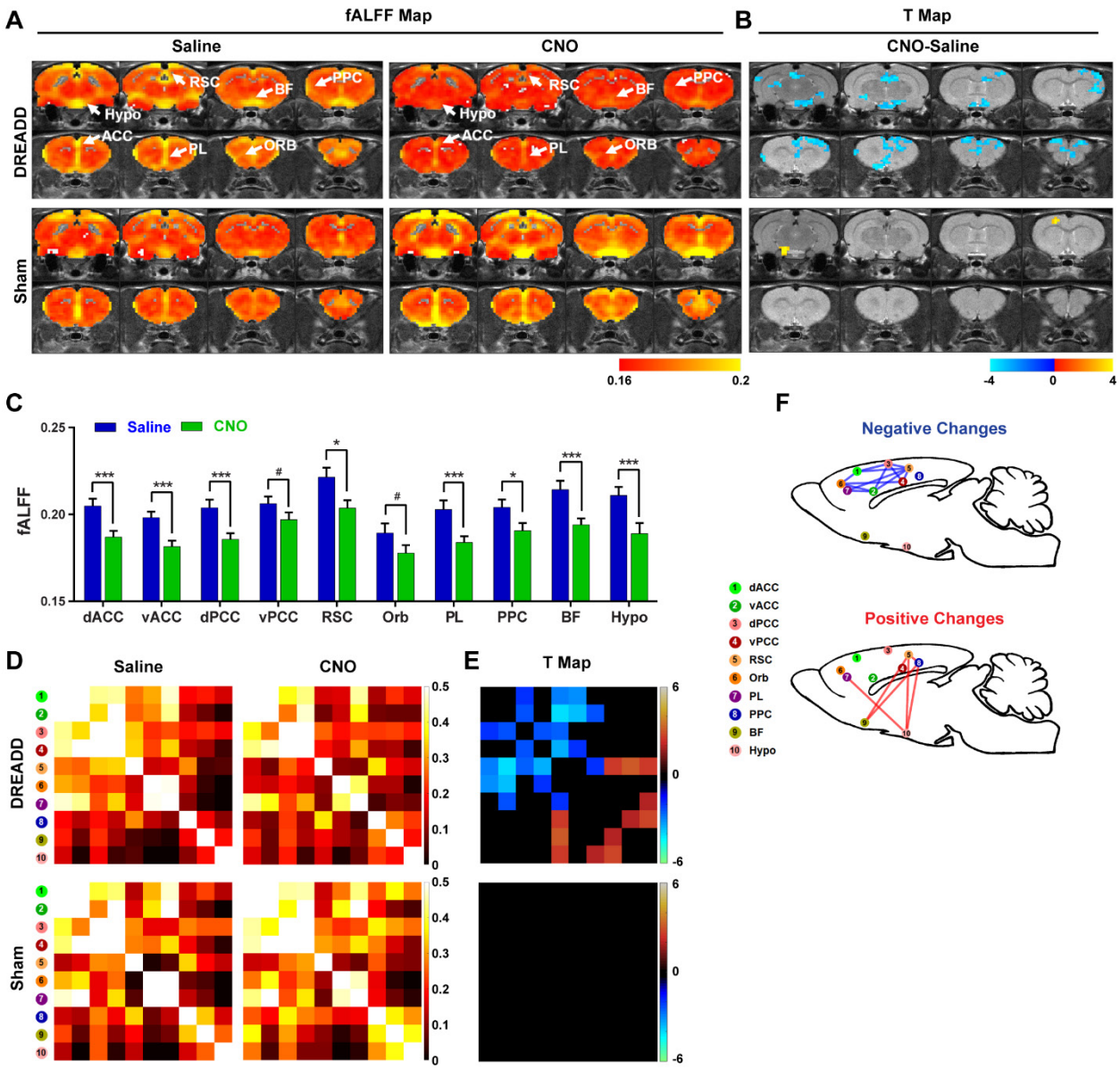

Figure 4. *Suppressing dACC disrupted activity across the DMN.* **A**) DMN constructed using fractional amplitude of low-frequency fluctuations (fALFF) after saline and CNO injections; **B**) Voxel-wise fALFF changes after DREADD inhibition ($p < 0.05$, linear mixed model, family-wise error corrected); C) ROI-wise fALFF changes after DREADD inhibition (*: $p < 0.05$; **: $p < 0.01$; ***: $p < 0.005$; #: $p = 0.11$). **D**) RSFC between DMN regions in the DREADD and sham groups after saline and CNO injections, respectively; **E**) RSFC changes between DMN nodes after dACC inhibition ($p < 0.05$, linear mixed model, FDR corrected); **F**) Negative and positive RSFC changes after dACC inhibition ($p < 0.05$, linear mixed model, FDR corrected).

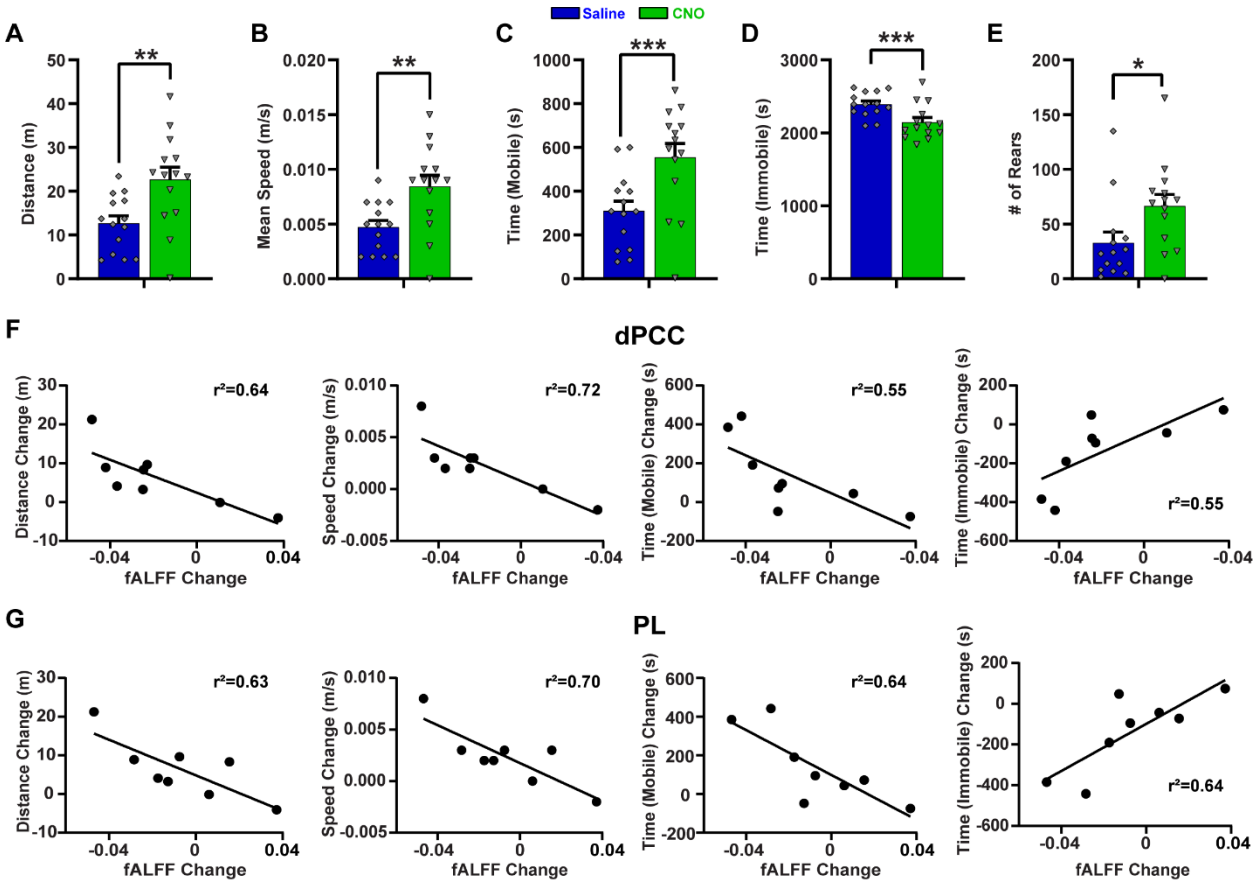

Figure 5. *Suppressing dACC changed DMN-related behavior (n=14).* **A**) Total distance traveled in homecage (45 min); **B**) Mean speed; **C**) Total mobile time; **D**) Total immobile time for at least 2s. **E**) Total rearing behavior. *: $p < 0.05$; ***: $p < 0.005$. **F**) Correlations of dPCC activity and DMN-related behaviors. **G**) Correlations of PL activity and DMN-related behaviors.

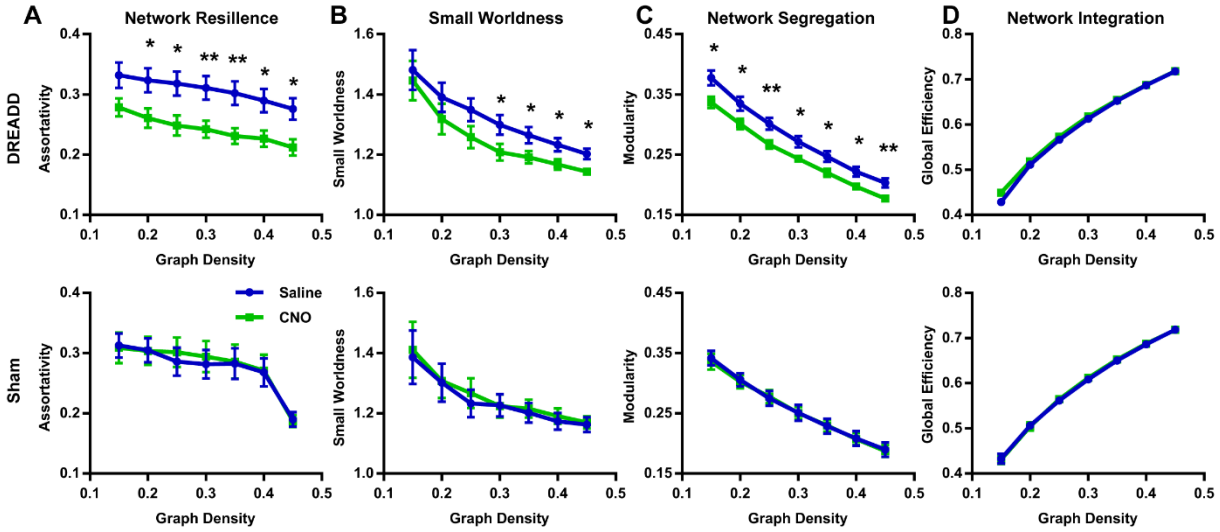

Figure 6. *Suppressing a hub node changed whole-brain network topology.* **A**) Network resilience; **B**) Small-worldness; **C**) Network segregation; **D**) Network integration. Linear mixed model; DREADD: n = 19, 78 scans; sham: n = 8, 41 scans. *: $p < 0.05$; **: $p < 0.01$.

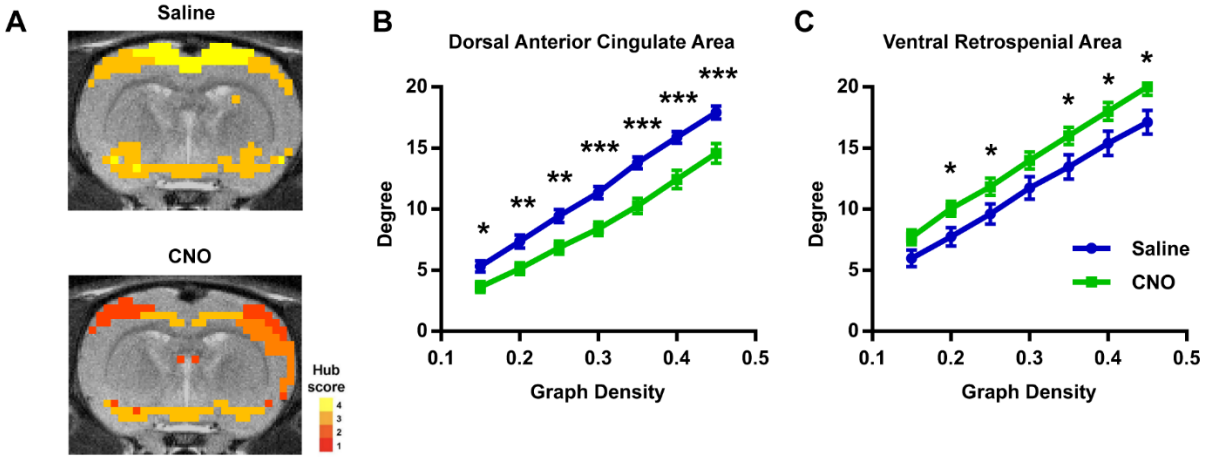

Figure 7. *New hub emerged after the inactivation of an existing hub*. **A**) Hub scores without and with dACC inactivation, respectively; **B**) The degree of dACC and ventral RSC without and with dACC inactivation (linear mixed model; n = 19, 78 scans). *: $p < 0.05$; **: $p < 0.01$; ***: $p < 0.005$.

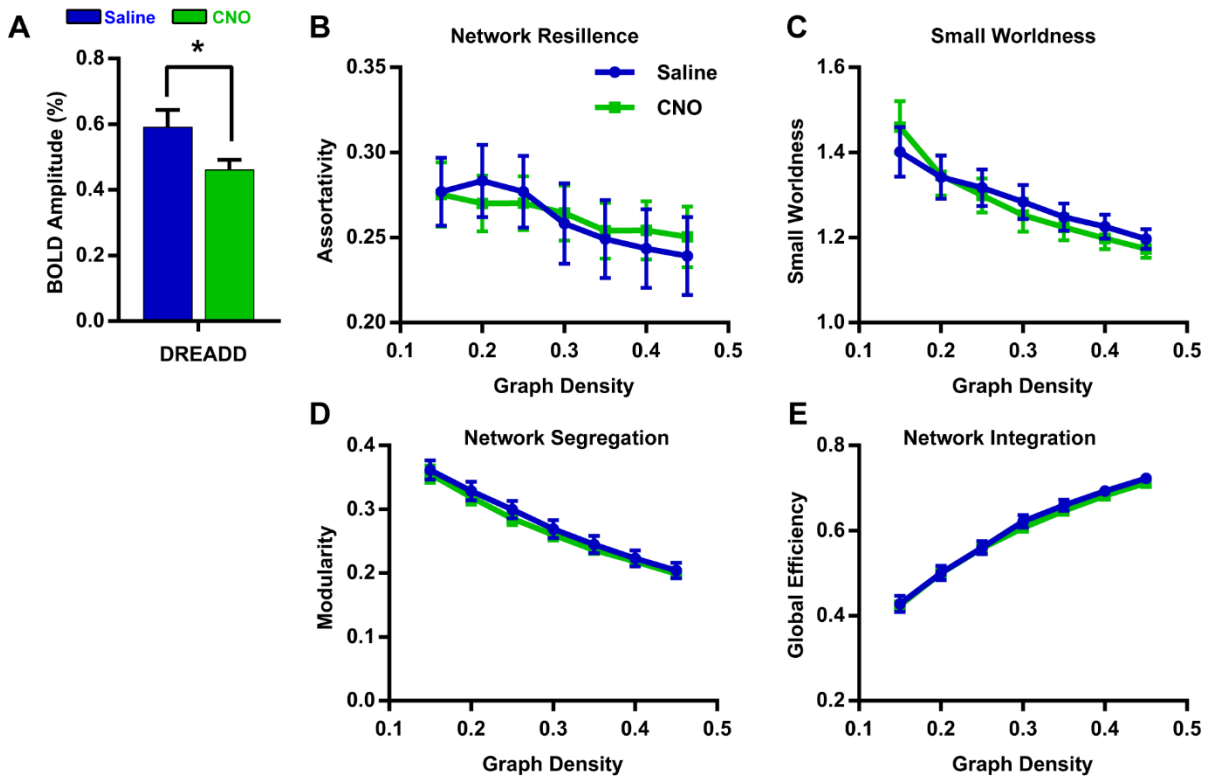

Figure 8. *Suppressing a non-hub node did not change whole-brain network topology.* **A**) Amplitude of spontaneous BOLD activity in the primary visual cortex after CNO and saline injections ($p < 0.05$, n=8, 66 scans); **B**) Network resilience; **C**) Small-worldness; **D**) Network segregation; **E**) Network integration.

How brain reacts to targeted attack at a hub region

Wenyu Tu[1], Zilu Ma[2], Yuncong Ma[2] and Nanyin Zhang[1,2]*

[1] Neuroscience Program, The Huck Institutes of the Life Sciences, The Pennsylvania State University, University Park, PA 16802, USA

[2] Department of Biomedical Engineering, The Pennsylvania State University, University Park, PA 16802, USA

***Address for correspondence:**

Nanyin Zhang, PhD

Professor of Biomedical Engineering and Electrical Engineering

Lloyd & Dorothy Foehr Huck Chair in Brain Imaging

The Huck Institutes of the Life Sciences

The Pennsylvania State University

W-341 Millennium Science Complex, University Park, PA 16802, USA

Email: nuz2@psu.edu

Supplementary Information

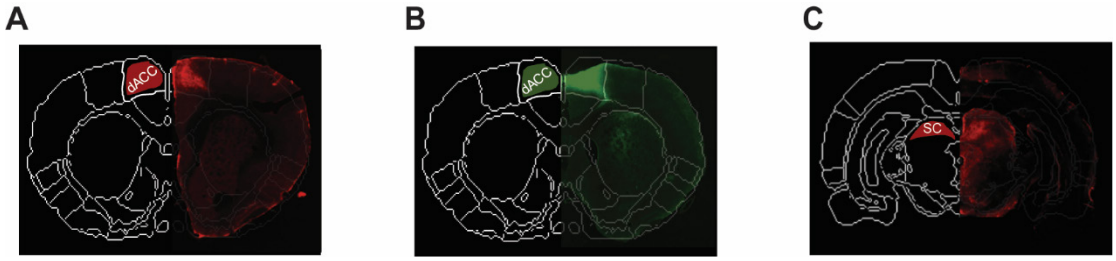

Figure S1. *Representative Histology.* Protein expression is shown in the right hemisphere. **A**) DREADD expression in the dorsal anterior cingulate cortex (dACC); **B**) GFP in the dACC (i.e. sham rats); **C**) DREADD in the superior colliculus. Anatomical definition is shown in the left hemisphere.

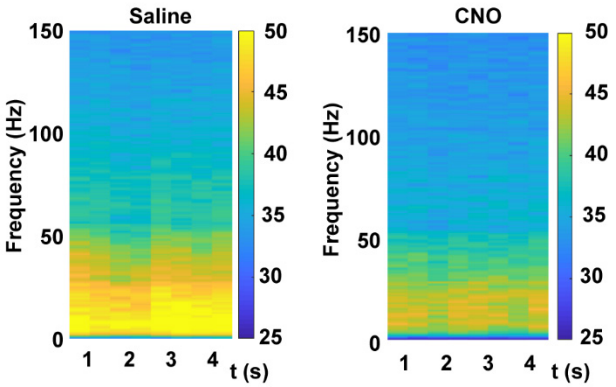

Figure S2. *LFP spectrograms after saline and CNO injections in a representative rat with DREADDs infused in the SC*.

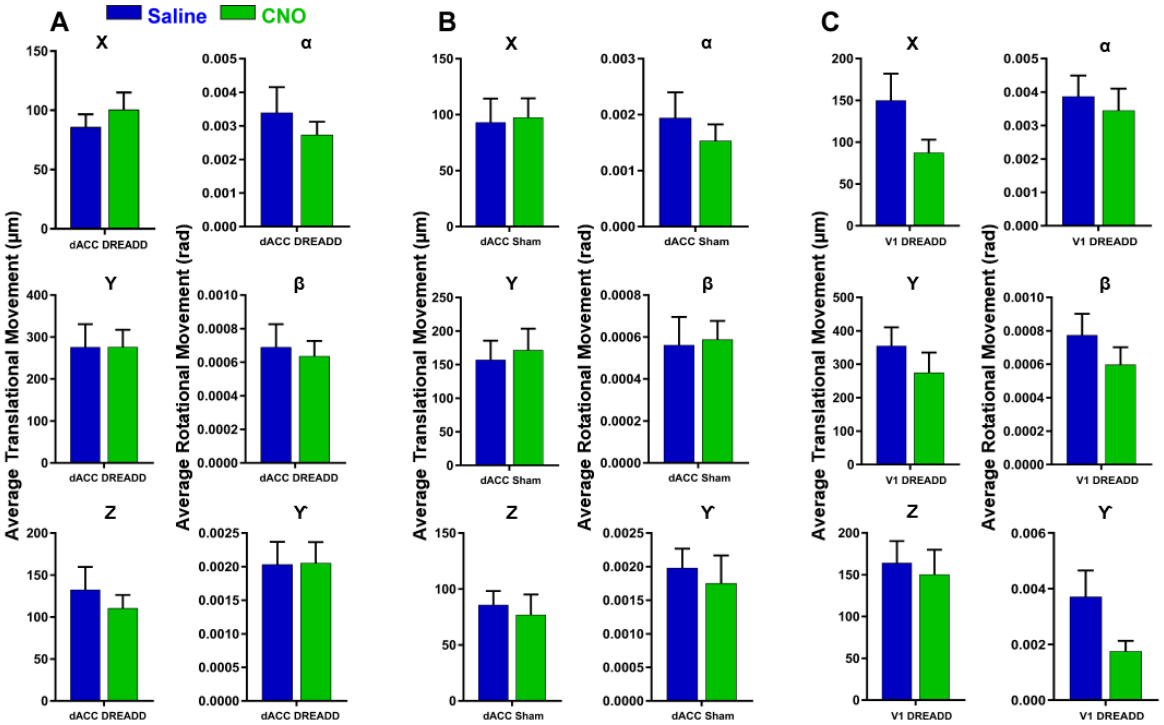

Figure S3. *Motion levels in all groups.* **A**. dACC DREADD (n=19, 78 scans); **B**. dACC sham (n=8, 41 scans); **C**. V1 DREADD (n=8, 66 scans). Left column: translational movement (in µm). Right column: rotational movement (in rad) (linear mixed model, $p > 0.05$ for all 6 parameters in all groups).

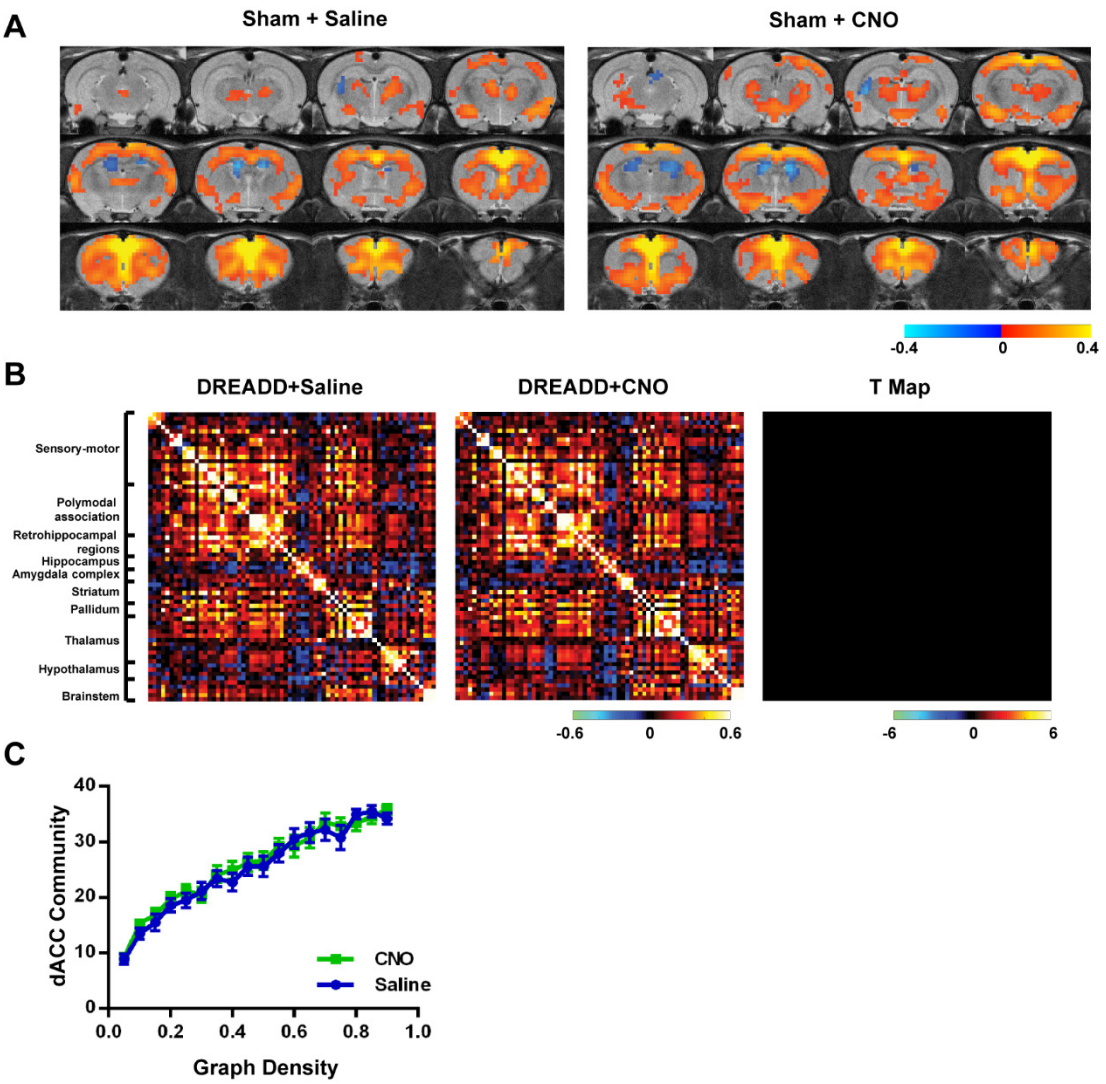

Figure S4. *Sham rats did not show reduced RSFC or dACC community size.* **A**) Averaged seedmaps after CNO and saline injections in the sham group (one sample t test, linear mixed model, $p<0.0005$, FDR corrected; n=8, 41scans); **B**) Averaged ROI-wise RSFC matrices after saline and CNO injections in the sham group. No connections exhibit RSFC changes (two-sample t-tests, linear mixed model, $p < 0.05$, FDR corrected). **C**) The size of the dACC-associated community as a function graph density after saline and CNO injections in the sham group (two-sample t-tests, linear mixed model, $p > 0.05$ for all densities tested).

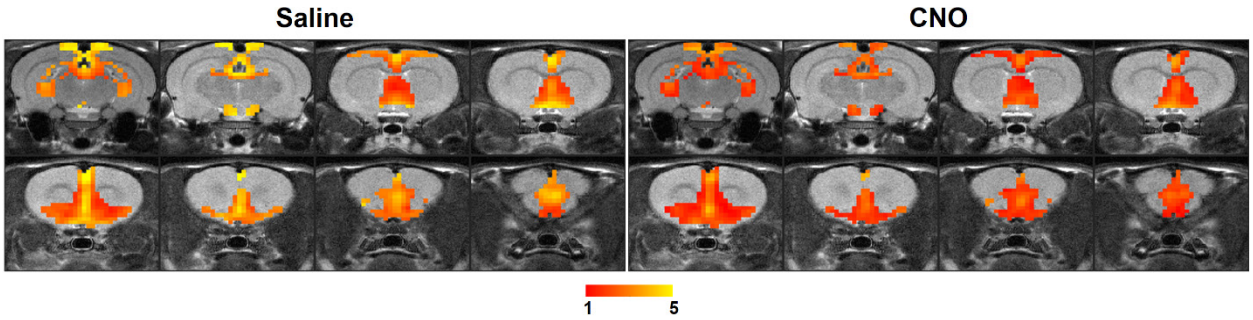

Figure S5. *DMN pattern revealed by independent component analysis.* rsfMRI data collected after saline and CNO injections were pooled together, and Group ICA was conducted. The DMN component was back projected to each group after group ICA.

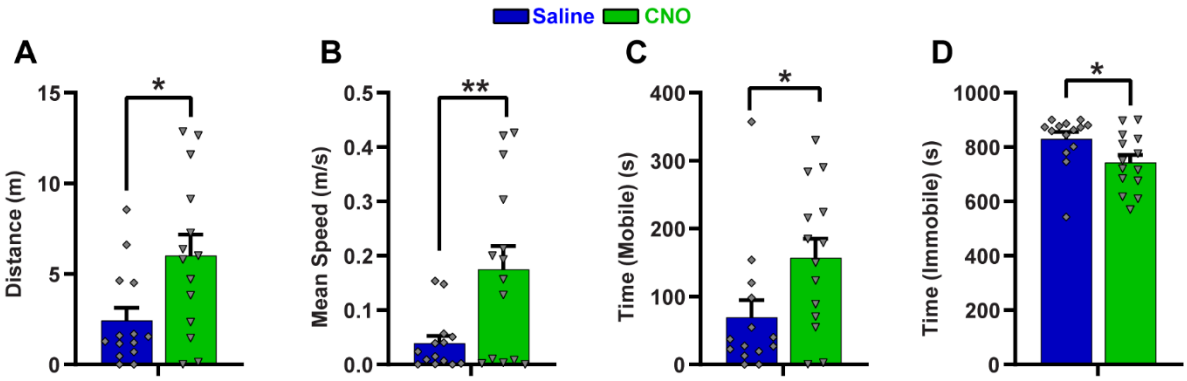

Figure S6. *Suppressing dACC changed DMN-related behavior (n = 14).* **A**) Total distance traveled; **B**) Mean speed; **C**) Total mobile time; and **D**) Total time when the animal was immobile for at least 2s in home-cage in the last 15 min of tests (i.e. 30 min after injection of CNO or Saline). *: $p < 0.05$, **: $p < 0.01$.

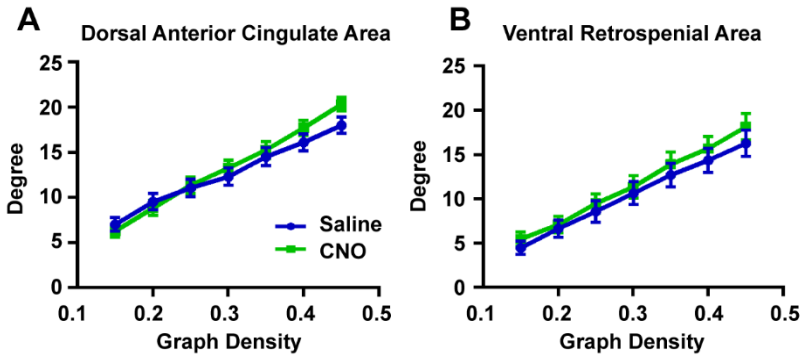

Figure S7. *Sham group did not show changed degree of dACC or RSC.* Degree changes of the dACC and ventral RSC in the sham group (two-sample t-tests, linear mixed model, $p > 0.05$ for all densities tested, n=8, 41 scans).

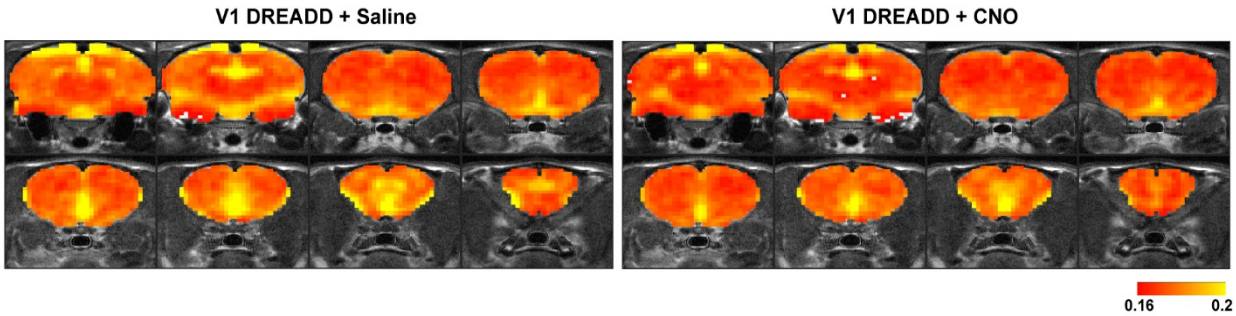

Figure S8. *Suppressing V1 did not affect DMN activity*. DMN constructed using fALFF in the V1 DREADD group after saline and CNO injections (n=8, 66 scans).

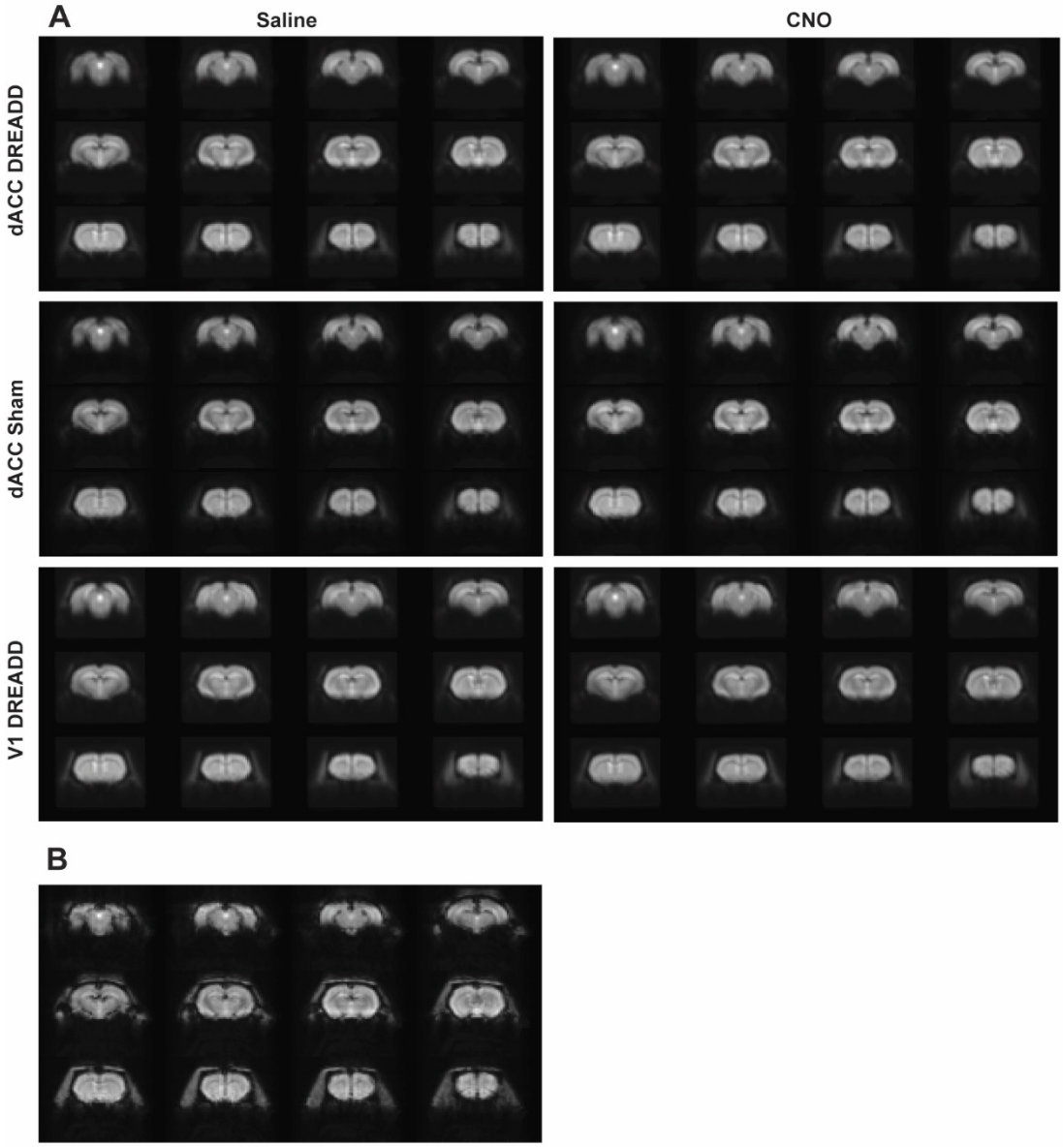

Figure S9. *Raw EPI data.* A. Averaged EPI image for each group and condition (dACC DREADD; dACC Sham; V1 DREADD); B. Example of a single EPI volume.